Journal of Applied Electrochemistry (2005) 35:139–149
DOI 10.1007/s10800-004-6207-7

The influence of microstructure on the corrosion rate of various carbon steels

D. CLOVER[1†], B. KINSELLA[1]*, B. PEJCIC[1] and R. DE MARCO[1]
[1]*WACRG, Department of Applied Chemistry, Curtin University of Technology, GPO Box U 1987, Perth, 6845, WA, Australia*
[†]*Present address: Baker Petrolite, Perth, WA, Australia*
*(*author for correspondence, fax: +61-8-9266-2300, e-mail: b.kinsella@curtin.edu.au)*

Received 14 June 2004; accepted in revised form 18 September 2004

Key words: carbon dioxide corrosion, corrosion resistance, carbon steel, microstructure

Abstract

This paper presents a fundamental study of the influence of carbon steel microstructure on the corrosion rate. Subsequently, the corrosion performance of various grades of carbon steels were evaluated in stirred autoclaves under elevated carbon dioxide and temperature conditions. Corrosion and penetration rates were determined via mass loss and optical microscopy, respectively. It was found that the corrosion rate of carbon steel line pipe is influenced by microstructure. More specifically, a relationship between localized corrosion susceptibility and the presence of pearlite bands in the steel microstructure was found. However, no correlation was evident between minor elemental concentrations (i.e., Ni, Cr, Mo) and corrosion resistance. It has been proposed that the corrosion stability of the various microstructures may arise from variations in the distribution of carbon bearing phases within the steel. In the banded ferrite/pearlite structure, the carbon-bearing phase (pearlite) is distributed in layers whereas in the other structures the carbon-bearing phases are much more evenly distributed. This study reports on the corrosion resistance of carbon steels in relation to their chemical and physical properties.

1. Introduction

The impact of carbon dioxide corrosion in the oil and gas industry is well recognized [1, 2]. The use of carbon steel in the pipelines of oil fields is dictated primarily by economic and strength reasons [3]. Subsequently, the corrosion rate of carbon steel is not only governed by the electrolyte conditions, but can also be influenced by its chemical composition and microstructure [4]. Furthermore, the driving force for corrosion in aqueous media is the difference in potential of small areas due to heterogeneities in the material [5]. It is important to note that these heterogeneities range from atomic to several hundred microns in scale, and can arise from various factors such as defects in the crystal structure of the metal, chemically different phases, segregation of elements or phases, non-metallic inclusions, *etc*. [5]. It is reported that many of these heterogeneities are controlled by the elemental composition, thermal and mechanical history of the material [5].

The successful use of carbon steel line pipe relies on appropriate design allowances and corrosion controls. Carbon steel line pipe used in oil/gas production and transmission, is manufactured in accordance with American Petroleum Institute (API) specification 5L, does not have a closely specified elemental composition and microstructure [6]. Consequently, it is fabricated to a set of mechanical requirements such as yield strength, tensile strength and fracture toughness. This can allow for significant variations in the elemental composition and microstructure, which can also influence corrosion performance. Although the specification emphasizes material strength and toughness, concentration limits of some elements (i.e., carbon, manganese, phosphorus and sulfur) are also specified to ensure weldability, formability and corrosion resistance [6]. However, the levels of alloying elements such as nickel, chromium and niobium, which may be added to the steel, are not specified. Furthermore, permitted levels of carbon, manganese, phosphorus and sulfur, which are specified for each grade may be different for seamless, welded and cold worked pipe. Similarly, the compositional and microstructural properties can vary significantly between pipes of the same grade from different manufacturers, and these variations may lead to substantial differences in the corrosion resistance of steel line pipe.

Recently, considerable effort has been devoted to understanding the corrosion mechanism and mitigation of mild steel in carbon dioxide environments [7, 8]. It is generally accepted that the partial pressure of carbon dioxide and temperature influence the corrosion rate according to the relationship described elsewhere [9, 10]. Various workers have proposed a reaction mechanism

that involves the formation of carbonic acid and its concomitant reduction [9, 11, 12]. Notwithstanding, the carbon dioxide corrosion mechanism is a convoluted process, which is influenced by many factors/conditions [2]. Various studies have shown that the steel microstructure plays a significant role in terms of the corrosion rate and mechanism [13–16]. Studies undertaken recently revealed that the inhibitor efficiency may also be influenced by the steel microstructure [17, 18]. Furthermore, Mishra et al. established an empirical relationship between carbon steel corrosion and microstructure [19, 20].

The general consensus is that the mechanism of carbon dioxide corrosion of carbon steel depends on a variety of factors [2]. Extensive research has been performed to understand this complex phenomenon; however, limited studies have investigated the influence of carbon steel microstructure on the corrosion rate under elevated carbon dioxide pressures and temperature conditions. Subsequently, the present study examines the extent of elemental composition and metallurgical variations in line pipe steel and their effect on corrosion performance. This paper attempts to investigate the corrosion behaviour of various grades of carbon steel. It is intended that this work will provide a more reliable prediction of the corrosion resistance of piping systems, noting that studies were performed in stirred autoclaves and were subjected to conditions similar to those encountered in the oil field.

2. Experimental details

2.1. *Sampling*

Samples were collected from various sources, and the details are provided in Table 1. The compositional limits for welded pipe are shown in Table 2 [6]. It is important to note that samples were compiled in order to enable comparisons between pipe of different grades and within particular grades. Subsequently, 34 line pipe and 2 tubing samples were obtained, 31 of these samples were characterized in terms of elemental composition and microstructure.

2.2. *Sample preparation*

Blocks of material approximately 25 mm square were cut from the supplied pipe samples by wet sawing. Coupons were fashioned from the blocks using electro discharge wire (EDW) cutting by S & G Precision Tools and Plastics (Perth, WA). The coupons were cut in the axial-tangential plane to ensure that the plane exposed during trials was similar to that exposed during pipe service. EDW cutting was chosen to minimize microstructural changes [21]. A Philips XL30 scanning electron microscope that incorporates an energy-dispersive analysis of X-rays (EDAX) accessory detected a small amount of copper and zinc contamination on the coupon surface, which arose from EDW. This layer was removed by polishing the coupons with wet 500 grit silicon carbide paper immediately prior to use. The samples were rinsed first with isopropanol followed by ethanol to remove any traces of grease.

2.3. *Gases and oxygen content*

The carbon dioxide was BOC food grade with a analysed oxygen content of <5 ppm. All test solutions were pre-sparged overnight and then for approximately and additional hour after transfer to the pressure vessel. The oxygen content was monitored using and Orbisphere Model 3655 portable analyser capable of measurements to 0.1 ppb. The measured concentration of dissolved oxygen, before pressurising was <3.6 ppb. Matheson Trigas, Research Purity methane (99.999%), was used for final pressurising. This gas has guaranteed oxygen content of <1 ppm.

2.4. *Corrosion testing*

All corrosion experiments were performed using a Parr 4522 bench top reactor with a 4843 temperature controller (2000 ml 316 stainless steel glass-lined pressure vessel) and temperature controller (Parr Instrument Company). The Parr setup comprises a motor drive that is magnetically coupled to a shaft in order to stir the solution contents. An Ashcroft digital gauge (model K2) was used to monitor the pressure. The steel coupons ($20 \times 10 \times 1$ mm) were attached to a Teflon holder secured to the lower end of the stirring shaftbelow a stirrer. A photograph showing the position of the Teflon holder and coupons inside the pressure vessel is given in Figure 1. A natural formation electrolyte obtained from an oil field was used in all tests, and the composition is provided in Table 3. All tests were performed using 1000 ml electrolyte at 50 °C and the coupons were rotated at 700 rpm for 2 weeks duration, unless stated otherwise. A carbon dioxide partial pressure of 3.4 bar was employed, with the total pressure of 21 bar being made up with methane. Corrosion rates were determined from mass loss measurements for corroded coupons that were cleaned in an inhibited Clarke's solution, whereas localized corrosion was measured by penetration depth using an Olympus PMG3 optical microscope. The latter method involved measuring the difference in focus (microns) between an un-corroded and a localized corroded area with the calibrated readings of the microscope. Five measurements were taken on each face of the coupon with the three deepest measurements, on each face, being averaged to obtain the penetration depth for that face. All experiments were carried out in triplicate.

Table 1. Sample details and supplier information

Sample number	Supplier	Manufacturer	Heat number	Grade	Size (OD × WT)
1	ABB	Dalmine	968034	ASTM A106-B	457.2 × 14.3
2	WOS	Sumitomo	J717122	ASTM A106-B	168.3 × 21.95
3	VL	Shin Ho	B-31954	API-5L GrB	115 × 6
4	VL	Shin Ho	A-08715	API-5L GrB	168.3 × 7.1
5	VL	Hyundai	A74181	API-5L GrB	168.3 × 7.9
6	VL	Hyundai	A-04753	API-5L GrB	406.4 × 12.7
7	VL	Hyundai	A98660	API-5L GrB	323.9 × 12.7
8	KAL	British Steel	5B82650	API-5L X56	508 × 15.9
9	KAL	Hyundai	B27704	API-5L GrB	273 × 9.8
10	AGL			API-5L X56	219.1 × 4.4
11	Epic	Kawasaki	5-82270	API-5L X65	406.4 × 9.4
12	Epic	NKK	X7478	API-5L X65	406.4 × 9.4
13	Epic	Nippon	ZL1202	API-5L X65	406.4 × 13.6
14	Epic	Marabeni	X7479	API-5L X65	406.4 × 13.6
15	Epic	Tubemakers	7221406	API-5L X70	406.4 × 8.8
16	Epic	Tubacero	752288	API-5L X65	406.4 × 9.4
17	Epic	Stupp	7047-0	API-5L X70	406.4 × 8.8
18	Nippon	Nippon	535733	API-5L X52	406.4 × 19.05
19	Nippon	Nippon	535711	API-5L X60	406.4 × 19.00
20	Nippon	Nippon	140497	API-5L GrB	406.4 × 12.00
21	Nippon	Nippon	140694	API-5L X42	323.9 × 25.40
22	Nippon	Nippon	140817	API-5L X65	323.9 × 31.75
23	TPS	Hyundai	A76150	API-5L GrB	323.9 × 9.5
24	TPS	Tubemakers	7308449	API-5L X42	273.1 × 9.3
25	TPS	Hyundai	ZC3839	API-5L GrB	219.1 × 8.2
26	Nippon	Nippon	141315	API-5L X65	273.1 × 19.05
27	Nippon	Nippon	ZE2711	API-5L X60	355.6 × 7.9
28	Nippon	Nippon	ZA1066	API-5L X52	355.6 × 8.7
29	Nippon	Nippon	ZB2316	API-5L X42	355.6 × 15.88
30	MEPA			L80	
31	MEPA			K55	
32	BHP	BHP	6340429	API-5L X42	219.1 × 4.8
33	BHP	BHP	6340089	API-5L X42	219.1 × 6.4
34	BHP	BHP	6340139	API-5L X42	219.1 × 8.2
35	BHP	BHP	6340588	API-5L X70	323.9 × 4.8
36	BHP	BHP	6292468	API-5L X70	323.9 × 8.4

Note that OD represents the outside diameter and WT signifies the wall thickness. ABB, ABB Engineering Construction Pty Ltd.; WOS, Westside Offshore Fabricators; VL, Van Leeuwen Pipe and Tube; KAL, K and A Laird (WA) Pty Ltd.; AGL, AGL Pipelines; Epic, Epic Energy Queensland Pty Ltd.; Nippon, Nippon Steel Australia Pty Ltd.; TPS, Tubemakers Piping Systems; MEPA, Mobil Exploration and Producing Pty Ltd.; BHP, BHP Structural and Pipeline Products.

2.5. *Metallurgical assessment*

Each sample was prepared by cutting three mutually perpendicular sections (axial–radial, radial–tangential and axial–tangential) followed by mounting in epoxy resin. Three sections of each sample were examined to assess directional character in the microstructure. Each mounted sample was wet ground to 500 grit on SiC paper with a Struers Dap-6 rotary polisher. The samples were diamond polished on Dap-6 in three stages as follows: (1) 15 μm diamond suspension on MD-Pan cloth with blue lubricant, (2) 6 μm diamond suspension on MD-Pan cloth with blue lubricant, and (3) 3 μm diamond suspension on MD-Mol cloth with red lubricant. A final colloidal silica polish was performed on MD-Chem cloth with OP-U suspension. The polished samples were etched in 2% nital (nitric acid in anhydrous methanol), with a 1:1 nital/picral (picric acid in anhydrous methanol) mixture being used for some higher carbon samples. Microstructural examination was performed using an Olympus PMG3 metallurgical microscope fitted with a 35 mm camera. The samples were characterized in terms of their elemental composition and microstructure.

3. Results and discussion

3.1. *Elemental composition*

Chemical analysis revealed that the elemental composition of the steel samples was very similar, with the exception of carbon, manganese and silicon (refer to Table 4). Subsequently, the carbon content decreased, whereas the manganese content increased with increasing strength. The silicon level varied between 0.1 and 0.2%, excluding the welded 5L-B samples, which had much lower silicon contents (<0.01%). It is worth noting that all samples did not contain significant levels of chromium, nickel and molybdenum, whereas the

Table 2. Chemical composition limits for API 5L line pipe

Grade	Type	Carbon%	Manganese%	Phosphorus%	Sulfur%
A25 Cl I	EW or CW	0.21	0.30–0.60	0.030	0.030
A25 Cl II	EW or CW	0.21	0.30–0.60	0.045–0.080	0.030
A	NE or CE	0.21	0.90	0.030	0.030
B	NE or CE	0.26	1.15	0.030	0.030
X42	NE or CE	0.28	1.25	0.030	0.030
X46, X52	NE	0.30	1.35	0.030	0.030
X46, X52	CE	0.28	1.25	0.030	0.030
X56, X60	NE or CE	0.26	1.35	0.030	0.030
X65	NE or CE	0.26	1.40	0.030	0.030
X70	NE or CE	0.23	1.60	0.030	0.030
X80	NE or CE	0.18	1.80	0.030	0.018

EW, Electric welded; CW, Continuous welded; NE, Nonexpanded; CE, Cold expanded specified limits are maximum values unless a range is given.

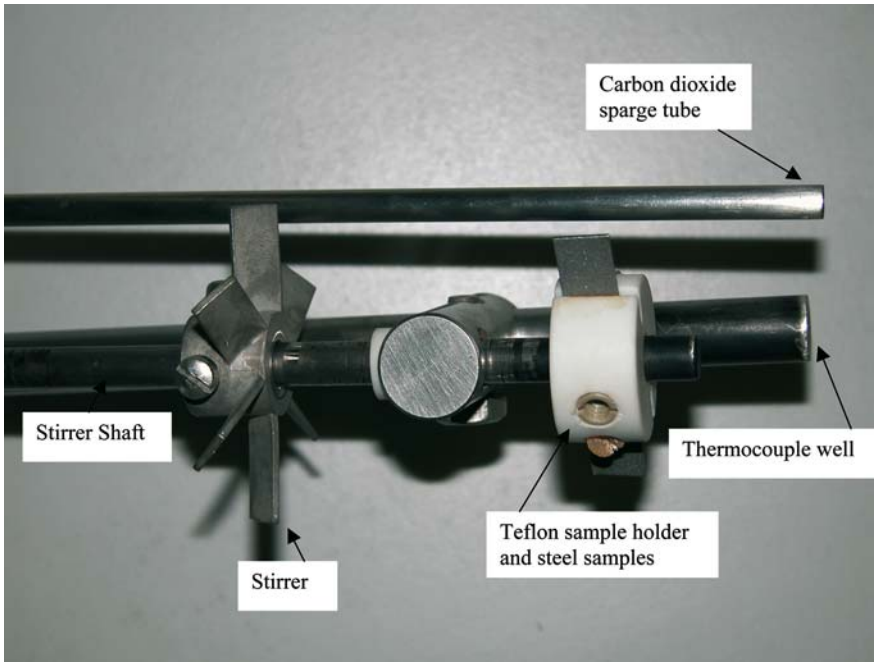

Fig. 1. Photograph of the inside of the autoclave vessel showing how the test metal specimens were attached.

Table 3. Formation water composition

Analysis and method	Composition
Conductivity	61 000 μS cm^{-1}
TDS by calculation	36 600 mg l^{-1}
Na^+ by AAS	12 000 mg l^{-1}
K^+ by AAS	185 mg l^{-1}
Ca^{2+} by AAS	400 mg l^{-1}
Mg^{2+} by AAS	200 mg l^{-1}
Cl^- by $AgNO_3$ titration	18 900 mg l^{-1}
CO_3^{2-} alkalinity by titration	Nil
HCO_3^- alkalinity by titration	320 mg l^{-1}
SO_4^{2-} by turbidmetry	5 mg l^{-1}

phosphorus and sulfur levels are well below the maximum limits set by the 5L specification. The higher X grade materials (X60 and above) comprised notable levels of the grain-refining elements niobium and vanadium. Titanium and aluminium, which are also known to refine grain size, were detected in some samples. Refining of the grain size is desirable since it is the only structural change that concurrently increases both strength and toughness [22].

3.2. *Microstructure*

It is important to note that the phases present are mainly determined by elemental composition, thermal and mechanical history [23]. The low carbon and alloy contents of these steels suggest that they can be expected to have predominantly ferritic microstructures [24]. Table 5 displays a summary of the various microstructures observed. It is clearly evident that the microstructure of only one line pipe sample appeared to have a

Table 4. Elemental composition of received samples

Sample number	Grade	C%	Si%	S%	P%	Mn%	Ni%	Cr%	Mo%	V%	Cu%	Ti%	Al%	Nb%
1*	A106-B	0.20	0.20	0.007	0.012	0.85	0.10	0.11	0.05	0.005	0.15	#	#	#
2*	A106-B	0.20	0.18	0.006	0.016	0.96	0.02	0.04	0.15	0.08	0.02	#	#	#
3	5L-B	0.13	0.01	0.005	0.012	0.63	0.01	0.01	#	#	0.01	<0.01	0.03	<0.01
4	5L-B	0.14	0.01	0.006	0.017	0.62	0.01	0.01	#	#	0.01	<0.01	0.02	<0.01
5	5L-B	0.16	0.01	0.007	0.015	0.62	0.01	0.01	#	#	0.01	<0.01	0.03	<0.01
6	5L-B	0.19	0.01	0.007	0.015	0.74	0.01	0.01	#	#	0.01	<0.01	0.03	<0.01
7	5L-B	0.18	0.01	0.009	0.019	0.73	0.01	0.01	#	#	0.01	<0.01	0.03	<0.01
8*	5L-X56	0.09	0.26	0.002	0.013	1.28	0.03	0.02	0.01	0.003	0.016	0.004	0.043	0.024
9	5L-B	0.16	0.02	0.006	0.013	0.76	0.01	0.01	#	#	0.01	<0.01	0.03	<0.01
10	5L-X56	0.07	0.19	0.004	0.017	1.05	0.02	0.02	#	0.02	0.01	<0.01	0.02	<0.02
11	5L-X65	0.07	0.20	0.005	0.018	1.44	0.02	0.03	#	0.04	0.01	<0.01	0.02	0.04
12	5L-X65	0.06	0.20	0.005	0.006	1.39	0.02	0.04	#	0.06	0.01	0.02	0.04	0.04
13	5L-X65	0.07	0.18	0.006	0.016	1.38	0.02	0.02	#	0.02	0.01	0.01	0.01	0.04
14	5L-X65	0.06	0.20	0.004	0.006	1.40	0.02	0.03	#	0.06	0.01	0.02	0.04	0.04
15	5L-X70	0.06	0.19	0.005	0.012	1.46	0.02	0.02	0.11	#	0.01	0.01	0.02	0.06
16	5L-X65	0.06	0.22	0.008	0.012	1.29	0.05	0.04	0.01	0.06	0.09	0.01	0.03	0.04
17	5L-X70	0.06	0.25	0.005	0.015	1.27	0.02	0.03	0.01	0.05	0.04	0.03	0.03	0.05
18	5L-X52	0.14	0.19	0.003	0.017	1.29	0.02	0.04	0.00	0.04	0.01	0.002	0.025	0.03
19	5L-X60	0.12	0.22	0.002	0.012	1.11	0.07	0.05	0.00	#	0.01	0.002	0.021	0.03
20	5L-B	0.19	0.18	0.006	0.018	0.62	0.03	0.04	0.00	0.03	0.02	#	0.002	#
21	5L-X42	0.12	0.22	0.002	0.012	1.11	0.07	0.05	0.00	#	0.01	0.002	0.021	0.03
22	5L-X65	0.07	0.22	0.001	0.010	0.86	0.03	0.04	0.19	#	0.02	0.013	0.029	0.03
23	5L-B	0.18	#	0.004	0.015	0.77	#	#	#	#	#	#	#	#
24	5L-X42	0.14	0.12	0.005	0.013	0.70	0.02	0.02	0.00	#	0.012	<0.003	#	<0.003
25	5L-B	0.17	0.18	0.004	0.018	0.55	#	0.01	0.02	#	#	#	#	#
26	5L-X65	0.07	0.19	0.002	0.008	1.27	0.03	0.03	0.22	#	0.01	0.002	0.033	0.03
27	5L-X60	0.09	0.18	0.002	0.017	1.34	0.02	0.03	0.00	0.003	0.01	0.001	0.023	0.032
28	5L-X52	0.10	0.23	0.003	0.012	1.02	0.02	0.02	0.00	0.001	0.01	0.017	0.019	0.03
29	5L-X42	0.09	0.23	0.006	0.009	0.97	0.02	0.03	0.00	0.001	0.02	0.001	0.027	0.017
32	5L-X42	0.14	0.13	0.004	0.015	0.73	0.021	0.022	0.002	#	0.011	0.003	0.037	<0.003
33	5L-X42	0.15	0.12	0.003	0.014	0.7	0.025	0.026	0.004	#	0.012	0.003	0.039	<0.003
34	5L-X42	0.13	0.13	0.004	0.013	0.72	0.23	0.017	0.003	#	0.012	0.003	0.047	<0.003

#, Not reported.

Table 5. Summary of microstructures, penetration and corrosion rates

Sample	Grade	CR via mass loss (mm y^{-1})	PR via depth of penetration (mm y^{-1})	Structure
Control		1.6	2.9	F, grain boundary carbides, GS:4
1	A106 B	2.2	6.0	F/P, P in coarse bands, GS:4
2	A106 B	1.5	5.7	F/P, P in coarse bands, GS:4
3	5L B	1.2	3.3	F/A/P, fine bands and scattered grains of P greater in center, GS:5 inner and outer edges have different microstructures
5	5L B	1.6	4.4	F/A, fine bands of small P grains through structure, GS:4
6	5L B	0.8	3.8	F/A, fine bands of small P grains through structure, GS:4
8	5L X56	1.0	4.1	F/P, P in bands of small grains, GS:4
9	5L B	1.0	6.0	F/A/P, numerous fine bands of small P grains through structure, GS:5
10	5L X56	1.0	3.9	F, small intergranular carbides F grains elongated, GS:8
11	5L X65	1.5	4.5	F, light etching bands, GS:8
12	5L X65	1.2	4.3	F/P, light etching bands, P grains small and scattered, GS:8
13	5L X65	1.2	4.4	F/P, light etching bands, small P grains in bands, GS:8
14	5L X65	1.1	5.2	F/P, light etching bands, small elongated grains of P, GS:7
16	5L X65	1.5	4.9	F, F grains elongated, GS:7
18	5L X52	1.0	5.8	F/P, P in evenly spaced bands of small grains, "pancake" structure, GS:5
19	5L X60	2.1	3.8	F/A
20	5L B	2.0	6.4	F/P, P in coarse bands, GS:3
22	5L X65	2.2	4.4	Tempered martensite
23	5L B	1.6	5.8	F/P, P evenly distributed, GS:6
26	5L X65	3.2	4.4	F, dispersed carbide, GS:7
31	5CT K55	2.0	4.6	Tempered martensite

CR, Average corrosion rate; PR, Penetration rate; F, Ferrite; P, Pearlite; A, Coarser and somewhat acicular Pearlite; GS, Grain Size – determined using an Olympus proprietary scale where GS 8 corresponds to an approximate average grain size of 2.4 μm, GS 7–5.6 μm, GS 6–6.8 μm, GS 5–14 μm and GS 4–20 μm.

non-ferritic structure (sample 22, tempered martensite). In the context of this paper three microstructures were most prevalent: (a) ferrite/pearlite; (b) ferrite/coarser and somewhat acicular pearlite/pearlite; and (c) fine-grained ferrite. Figure 2 shows an example of the various microstructures observed in this study.

3.3. *A106 B samples*

Two samples (i.e., 1 & 2) of pipe conforming to ASTM A106 grade B were obtained, noting that these were made by the seamless process. Sample 1 had no visible inclusions, whereas sample 2 had some oxide inclusions near the outer surface. The microstructure in both specimens consisted of coarsely banded ferrite/pearlite in a banded arrangement [24]. These layers which are one or more grains thick appear parallel to the axis of the pipe and perpendicular to its radius. Apparently the banding was dominant in the axial direction due to the greatest amount of deformation occurring in this direction as a result of the manufacturing process. The banded microstructure is produced by preferential formation of pearlite along bands rich in manganese. Cast steel normally solidifies with a dendritic structure, and as the steel cools, elements with lower solubility in austenite segregate to the interdendritic regions [22]. During forming of the steel into finished pipe, the segregated regions are elongated in the direction of deformation, resulting in the formation of layers rich in the segregated elements. Electron probe microanalysis (EPMA) results shown elsewhere revealed that the segregated elements are mainly manganese and silicon [24].

Energy dispersive (EDAX) spectra were collected to further examine the composition of sample 2, and this revealed manganese segregation. Figure 3 shows the variation in manganese content at 10 μm intervals perpendicular to the direction of banding. Unfortunately, silicon segregation could not be detected under these conditions and is probably below the detection limit of EDAX. The banded structure observed here appears to be more prevalent in seamless material, probably due to the smaller amount of deformation that occurs during the manufacture of seamless pipe. Deformation during the first stages of hot working causes the elongation of segregated regions resulting in the banded structure; however, further deformation has a homogenizing effect on segregated steels [22]. Subsequently a more heavily worked material is likely to be more homogenous and not display the effects of segregation such as the banded structure.

3.4. *API 5L B samples*

Eight (samples 3, 4, 5, 6, 7, 9, 23 & 25) of the nine API 5L B samples exhibited the ferrite/coarser, and somewhat acicular pearlite/pearlite microstructure. The for-

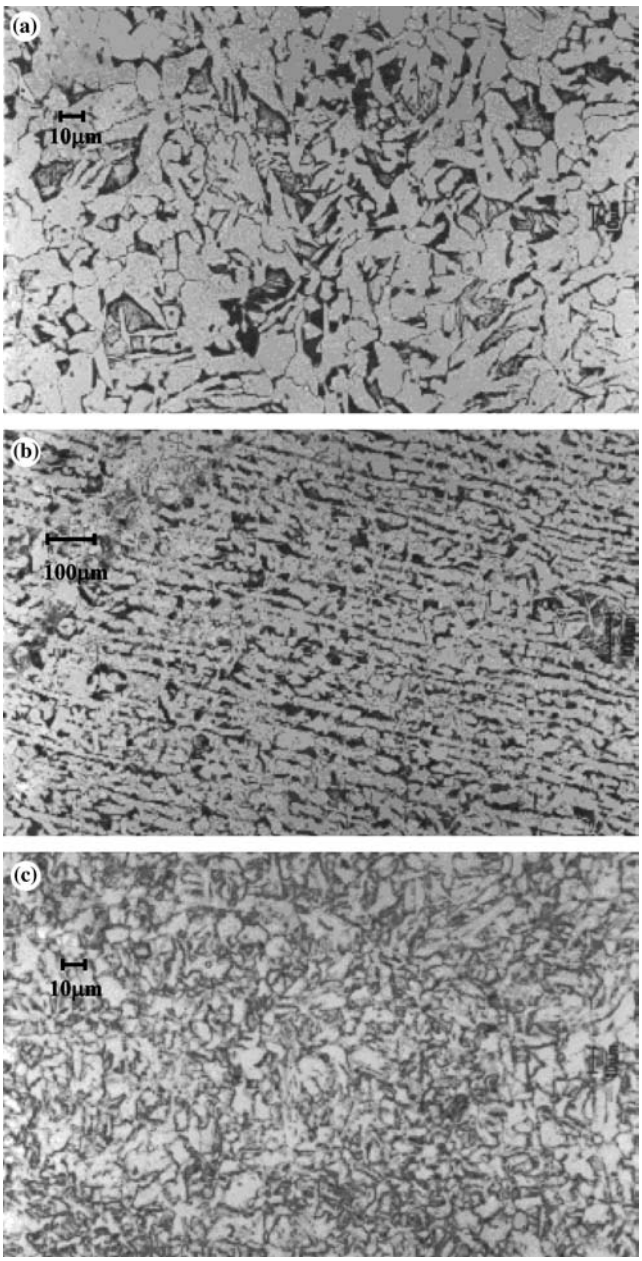

Fig. 2. Photographs taken of the various forms of carbon steel microstructure (a) coarse ferrite and pearlite, somewhat acicular (sample 6), (b) banded ferrite/pearlite (sample 12), and (c) ferrite with some dispersed carbide (sample 15). Note, the magnification bars are included in the middle of the right-hand side of each micrograph, and (a) and (c) possess magnification bars of 10 μm, while (b) has a magnification bar of 100 μm.

mation of coarser pearlite is reported to be promoted by the presence of manganese [24]. The API 5L B samples had varying ratios of pearlite and coarser and acicular pearlite. Samples with a larger proportion of finer pearlite had a corresponding smaller proportion of coarser pearlite, because both phases contain carbon. Apparently sample 3 displayed a dramatic variation in microstructure through the thickness of the pipe wall. Subsequently the inner edge consisted of coarser pearlite in a matrix of ferrite with only a small number of very fine pearlite grains, whereas the centre consisted of lines

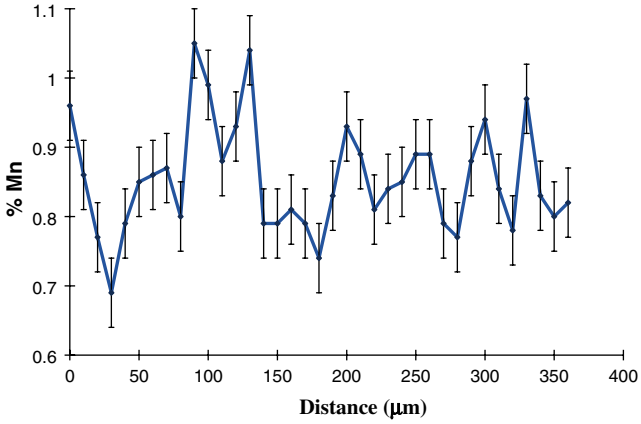

Fig. 3. Variations in the manganese content of sample 2 as a function of distance.

of fine pearlite grains in a ferrite matrix along with a few scattered coarser pearlite grains. The outer edge contained small evenly distributed grains of pearlite in a ferrite matrix.

Conversely, the structure of samples 4, 5, 6, 7 & 9 comprised mostly ferrite and coarser/acicular pearlite. Sample 4 contained elongated voids at the centre of the cross section, while sample 5 had elongated voids and lines of inclusions. Sample 6 comprised lines of small grains/inclusions, whereas no inclusion bands were evident in sample 7. By contrast, sample 9 had numerous fine streaks of inclusions throughout its ferrite/coarser, and somewhat acicular pearlite structure. The ferrite/coarser and somewhat acicular pearlite/pearlite structure of sample 23 contained lines of fine inclusions and some porosity, whereas sample 25 had some lines of small grains throughout its ferrite/coarser and somewhat acicular pearlite structure. The microstructure of sample 20 was in general very similar to the ASTM A106 B samples; however, an alternate layer of ferrite and the banded pearlite structure was evident. Subsequently, no visible inclusions were detected in sample 20.

3.5. *API 5L X42 samples*

Three samples (i.e., samples 21, 24 & 29) of this grade had ferrite/pearlite microstructures consistent with a normalising treatment. It is well known that normalising is a heat treatment process where steel is austenitised before being allowed to cool in air, and this process generates a microstructure of equiaxed ferrite and pearlite. Subsequently, these samples had a smaller pearlite volume fraction and a more fine grain size compared to grade B samples with a similar microstructure. The smaller pearlite volume fraction is commensurate with their lower carbon content, whereas the grain size is most likely obtained by control of the rolling/heat treatment processes, noting that the concentration of grain-refining elements was low. It is worth mentioning that samples 21 and 29 were from welded pipe, whereas sample 24 was from seamless pipe. Both

welded samples had a banded-type structure, symbolic of manganese segregation, with the pearlite occurring in fine bands of small grains. The seamless sample had a larger grain size compared to the other two samples, noting that the pearlite was uniformly distributed within the ferrite matrix. No inclusions were visible in any of these samples.

3.6. *API 5L X52 samples*

The API 5L X52 grade consisted of two samples (i.e., 18 & 28), noting that sample 18 was a seamless pipe, whereas sample 28 was obtained from a welded pipe. The microstructure of sample 18 was consistent of ferrite and pearlite in a banded arrangement similar to the ASTM A106 B samples. However, the amount of pearlite present was significantly lower, and the grain size was much finer compared to the ASTM A106 B steels. The microstructure of sample 28 consisted of small-elongated pearlite grains in a matrix of fine ferrite, with several elongated voids visible in the centre of the cross section. Apparently, this microstructure is similar to the API 5L X65 and X70 samples (as discussed in Section 3.8).

3.7. *API 5L X56 and X60 samples*

Four samples of this grade were examined (i.e., 8, 10, 19 & 27), noting that sample 19 was from welded pipe, while the others were from seamless pipe. Both samples 8 and 27 consisted of ferrite/pearlite microstructures, and evidence of a banded-type arrangement was not particularly evident. Nevertheless, sample 8 had a larger grain size compared to the other samples of this group. Evidently, sample 27 contained large voids elongated in the rolling direction, and the grain size was substantially larger in the centre compared to near the edge. In addition, the presence of pearlite at the centre of this sample was apparent. Sample 10 contained intergranular carbides distributed in bands in a fine ferrite matrix, and some small equiaxed pores were also visible. By contrast, the microstructure of sample 19 comprised fine-grained ferrite with a coarser, and somewhat acicular pearlite with a modest amount of small equiaxed pores.

3.8. *API 5L X65 and X70 samples*

The microstructures of nine API 5L X65 and X70 samples of pipe (i.e., 11, 12, 13, 14, 15, 16, 17, 22 & 26) were investigated. Samples 11 to 17 were from coated, welded pipe intended for use in natural gas pipelines, whereas samples 22 and 26 were from uncoated seamless pipe. Although the steels were obtained from different manufacturers, the coated samples had very similar microstructures. In particular, they consisted of primarily fine-grained ferrite with a modest amount of pearlite, and in some cases carbides. Bands of material that etched lighter than the bulk was also present, noting that these bands contained ferrite. No inclusions or pores were visible in any of these samples. By contrast, the structure of sample 22 consisted of tempered martensite, and contained some porosity. Unfortunately, the microstructure of sample 26 could not be assigned due to its complicated nature; however, it appears that it most likely consists of ferrite and tempered coarse grained pearlite.

3.9. *Corrosion and penetration rates*

The corrosion and penetration rates of the carbon steel samples have been summarized in Table 5. Subsequently, the corrosion rates ranged between 0.8 and 3.2 mm y^{-1}, noting that most were in the range of 1.0–1.5 mm y^{-1}. By contrast, the penetration rates varied between 3.3 and 6.4 mm y^{-1}, and there appeared to be no evidence of a relationship between the penetration-corrosion rates. Notwithstanding, the penetration rates were significantly higher. Generally, the penetration rates for samples with low carbon content (i.e., $<0.10\%$) appeared to be slightly lower (3.9–5.2 mm y^{-1}) compared to those with elevated carbon contents (3.3–6.4 mm y^{-1}). However, as the low carbon content samples are confined to the higher-grade material and generally had different microstructures, it is not certain whether this effect is attributable to carbon content or microstructure. Furthermore, no correlation between elemental composition and corrosion rate was clearly visible. This is partly due to the samples having almost similar compositions and low levels of alloying elements.

3.10. *Corrosion mechanism*

Five distinct corrosion forms were observed on the line pipe steel coupons, and these have been identified as follows: uniform; sharp line form; soft line form; mesa; and pitting. Table 6 displays the various forms of corrosion witnessed on each of the steel specimens after exposure to the electrolyte. It is worth noting that the sharp line corrosion appeared in the form of distinct, closely spaced, parallel ridges, whereas the soft line form consisted of more widely spaced, smaller aspect ratio, parallel ridges. The mesa form exhibited small-unreacted areas surrounded by regions in which corrosion had occurred. Apparently, the coupons displayed some form of localized attack, with the mesa type being the most prevalent. The protection of the unreacted areas could be due to adsorbed species from the fluid acting as inhibitors and/or by a thin layer of adherent scale. It is important to note that $\sim$70% of the coupons experienced elevated corrosion rates at the edges and at the central area of the trailing face, and this is attributed to these portions being exposed to more turbulent conditions compared to the rest of the coupon. Another reason for the high corrosion rates in these regions could be due partly to the removal of corrosion products/protective films as a result of the enhanced mass transport. The flow patterns observed on the

Table 6. Corrosion forms observed on the various steel specimens

Sample	Grade	Leading face corrosion form	Trailing face corrosion form	Flow Effects
Control		Uniform	Uniform	Some regions on trailing face revealed no significant levels of corrosion, leading face slightly less corroded in center.
1	A106 B	Mesa/soft line form, parallel and at 45° to long axis	Soft line form	Centre area of leading face was less corroded, edges of leading face were more heavily attacked. The trailing face was only attacked in the central region.
2	A106 B	Mesa	Pitting	Edges of the leading face were more heavily attacked. Main attack on the trailing face was in the central region.
3	5L B	Soft Line form/mesa	Soft line form	Replicate A was evenly attacked over the leading face, whereas replicate B had a large area centrally located on the leading face that was not attacked. The trailing face was attacked predominantly in the central region.
5	5L B	Mesa/soft line form	Soft line form	Islands formed on trailing face by mesa corrosion were elongated in the predicted flow direction.
6	5L B	Sharp line form	Localised sharp line form	The central region of the leading face was less corroded.
8	5L X56	Mesa	Uniform	The central area of the leading face was less attacked. Attack on the trailing face was in the center.
9	5L B	Soft line form/mesa	Soft line form	Edges of leading face more heavily attacked, with little attack in the central region. Attack on trailing face occurred predominantly in the central region.
10	5L X56	Mesa	Very little attack	Islands formed on leading face by mesa corrosion were elongated in the predicted flow direction and attack was less severe in the center.
11	5L X65	Soft line form/mesa	Soft line form	The mesa area on the leading face was centrally located. Main attack on the trailing face was in the central region.
12	5L X65	Soft line form	Very little attack	None observed.
13	5L X65	Mesa/soft line form	Uniform	The central area of the leading face was less attacked. Attack on the trailing face was in the center.
14	5L X65	Mesa	Soft line form	Less attack in the central region of leading face.
16	5L X65	Mesa/soft line form	Soft line form	Attack on trailing face in central region.
18	5L X52	Mesa	Pitting	Central region of leading face less attacked. Trailing face attacked only in central region.
19	5L X60	Mesa	Uniform	Islands of material formed by mesa corrosion on leading face elongated in the direction of fluid flow. Attack on trailing face in central region.
20	5L B	Mesa	Uniform	Edges of leading face more heavily attacked. Attack predominantly in center of trailing face.
22	5L X65	Uniform/mesa	Pitting	The mesa region was centrally located on the leading face. Only the edges and central area of the trailing face were attacked.
23	5L B	Mesa	Very little attack	Islands formed by mesa corrosion on the leading face are elongated in the flow direction
24	5L X42	Mesa	Mesa	Central area of leading face not as heavily attacked. Only a small central region of attack on the trailing face.
25	5L B	Mesa/soft line form	Very little attack	The edges were heavily attacked.
26	5L X65	Uniform	Uniform	None observed.
31		Uniform/micro-pitting	Uniform/micro-pitting	None observed.

coupons have been termed flow effects and are summarized accordingly in Table 6.

The ridges that formed on the coupons in line form corrosion were parallel to the long axis of the pipe. During pipe manufacturing (either seamed or seamless), the material flow is greatest along the pipe axis. Consequently, any heterogeneous regions that are elongated in this direction may produce corroded ridges by one of the following mechanisms; (a) local anodes and cathodes may be formed due to electrochemical differences between adjoining regions, and/or (b) scale may adhere preferentially to particular regions, due to factors

such as carbide distribution, causing localized attack. Presumably, galvanic couples form between carbon-rich phases and the bulk steel, noting that cementite is cathodic with respect to iron. Similarly, manganese is more anodic compared to iron, and this may favour the formation of a galvanic couple between the manganese-rich region and the bulk material. Obviously, these two effects would compete against each other as manganese-rich regions preferentially contain carbon-bearing phases. Manganese is also known to influence the formation of carbon bearing phases in steel, noting that areas enriched with manganese have a tendency to preferentially form pearlite. It is reported that carbide morphology effects scale adhesion [4]. Perez et al. (1996) suggested that cementite is able to anchor scale by a mechanical keying process [4]. Layers or platelets of cementite form on the surface of pearlitic steel due to preferential corrosion of the ferrite in pearlite grains (pearlite is a lamellar structure of cementite, Fe_3C; and ferrite, Fe). Subsequently, iron carbonate scale becomes trapped between these platelets, and this tends to form a physical barrier between the electrolyte and the steel. However, non-uniform coverage of the surface with scale may favour localized corrosion.

3.11. *The metallurgy/corrosion relationship*

In order to establish a microstructure–corrosion relationship, it was deemed necessary to arrange the carbon steels into various groups. Consequently, the samples were categorized according to four groups as follows

Group 1: banded ferrite/pearlite microstructure (samples 1, 2, 18 and 20)

Group 2: very fine predominantly ferrite microstructure (samples 10, 11, 12, 13, 14, 16 and 26)

Group 3: ferrite/coarser, and somewhat acicular pearlite/pearlite microstructure (samples 3, 5, 6, 9 and 23)

Group 4: tempered martensite microstructure (samples 22 and 31)

It is worth noting that all of the other samples were not categorized, since they did not meet any of the above classifications.

Table 7 displays the penetration and corrosion rate results for each of the microstructure groups. It is clearly evident that group 3 revealed a lower mean average corrosion rate compared to group 4, and this is probably due to the higher free energy of the metastable martensite phase. Apparently, the penetration rates within group 3 varied considerably that the samples were classed according to sub-groups. The first sub-group comprised penetration rates of 3.3–4.4 mm y^{-1}, whereas the second had penetration rates of between 5.8 and 6.0 mm y^{-1}. Unfortunately, the data reported in this paper do not provide an unequivocal relationship between the corrosion rate and microstructure of carbon steel alloys. Notably, the absence of a clear-cut relationship between corrosion rates observed within groups 1 and 2 with a wide range of microstructures is consistent with this assertion. However, it is worth noting that the penetration rates of group 1 were statistically higher. Subsequently, the carbon-bearing phase in group 1 is due to pearlite (a lamellar structure of cementite and ferrite), which is distributed as layers and associated with manganese. The carbon steels of groups 2, 3 and 4, although having different microstructures, appeared to have a more uniform distribution of cementite. In these groups, the cementite was found in several phases, including coarser, and somewhat acicular pearlite, martensite, and discrete carbides. The difference witnessed between carbon steels with segregated and evenly distributed cementite-containing phases, implies that the distribution of cementite is responsible for the variation in corrosion performance. This is consistent with suggestions made elsewhere that the shape and distribution of ferrite/Fe_3C plays an important role in influencing the corrosion rate [20]. Recent studies have shown that long exposure times lead to an increase in the corrosion rate, and this was attributed to an elevated Fe_3C surface area [25].

4. Conclusions

This study has shown that the localized and general corrosion rates vary slightly between different carbon steels. Furthermore, the line pipe steels investigated in this paper revealed corrosion rate variations of 0.8–3.2 mm y^{-1} and 3.3–6.4 mm y^{-1} for the general and localized forms, respectively. It has been shown that variations in the corrosion/penetration rate occur partly due to differences in the microstructure. It was found that steels with a banded ferrite/pearlite structure perform poorly in terms of localized corrosion and this was attributed to a segregated distribution of the iron carbide phase cementite (Fe_3C). By contrast, all other microstructural types were observed to have a uniform distribution of cementite. Insignificant differences were observed in the corrosion performance of steels having

Table 7. Corrosion resistances of the steel specimens grouped according to microstructure

Microstructural group (N° of samples in group)	Mean penetration rate (Range) mm y^{-1}	Mean average corrosion rate (Range) mm y^{-1}
Group 1 (4)	6.0 (5.7–6.4)	1.7 (1.0–2.2)
Group 2 (7)	4.5 (3.9–5.2)	1.5 (1.0–3.2)
Group 3 (5)	4.7 (3.3–6.0)	1.2 (0.8–1.6)
Group 4 (2)	4.5 (4.4–4.6)	2.1 (2.0–2.2)

fine-grained ferrite, ferrite/coarser, and somewhat acicular pearlite/pearlite or tempered martensite microstructures. In any event, the ferrite/coarser, and somewhat acicular pearlite/pearlite material performed better in terms of both the average corrosion and penetration rates. It is suggested that a ferrite/coarser, and somewhat acicular pearlite/pearlite structure may be more suitable under the conditions investigated in this study compared to a coarse banded ferrite/pearlite structure. This paper has demonstrated that steel microstructure is an important consideration when selecting a grade B pipe material for a particular application.

Acknowledgements

The authors thank the Minerals and Energy Research Institute of Western Australia (MERIWA) for funding this project (Project No. M287).

References

1. NACE Task Group, T-1-3 (Ed.), '*Introduction, in CO2 Corrosion in Oil and Gas Production-selected Papers, Abstracts and References*' Vol. 3 (NACE, Houston, Texas, 1984).
2. A.M.B.M. Kermani, *Corrosion* **59**(8) (2003) 659.
3. W.R. Revie (Ed.), 'Uhlig's Corrosion Handbook', 2nd edn. (John Wiley & Sons, 2000).
4. T. Perez, G. Fitzsimons and K.Videm, Proceeding of the 13th International Corrosion Conference, Melbourne (1996).
5. L.L. Shreir, R.A. Jarman and G.T. Burstein, 'Corrosion' (Oxford, Butterworth-Heinemann, 1994).
6. American Petroleum Institute, 'API Specifications 5L', 41st edn. (1995).
7. Y.J. Tan, 'Electrochemical studies on carbon dioxide corrosion and its inhibition', Ph.D. Thesis, Curtin University, Perth, Australia (1996).
8. W.H. Durnie, Ph.D. Thesis, Curtin University, Perth, Australia (2000).
9. C.M. de Waard and D.E. Milliams, *Corrosion* **31**(5) (1975) 131.
10. C.L. de Waard, U. Lotz and D.E. Milliams, *Corrosion* **47**(12) (1991) 976.
11. G.R.B. Schmitt, G, *Part 1: Kinetics of the liberation of hydrogen*, Werkstoffe und Korrosion **28** (1977) 816.
12. G.I.W. Ogundele and W.E. White, *Corrosion* **42**(2) (1986) 71.
13. K. Videm, J. Kvarekvaal, T. Perez and G. Fitzsimons, *Corrosion* (*NACE International 96*) Paper No. 1 (1996) 1.
14. H. Asahi, T. Kushida, M. Kimura, H. Fukai and S. Okano, *Corrosion* **55**(7) (1999) 644.
15. A. Dugstad, H. Hemmer and M. Seiersten, *Corrosion* **57**(4) (2001) 369.
16. V.A. Alves, C.M.A. Brett and A. Cavaleiro, *J. Appl. Electrochem.* **31** (2001) 65.
17. D.A. Lopez, W.H. Schreiner, S.R. de Sanchez and S.N. Simison, *Appl. Surf. Sci.* **207** (2003) 69.
18. D.A. Lopez, S.N. Simison and S.R. de Sanchez, *Electrochimica Acta* **48** (2003) 845.
19. B. Mishra, S. Al-Hassan, D.L. Olson and M.M. Salama, *Corrosion* **53**(11) (1997) 852.
20. S. Al-Hassan, B. Mishra, D.L. Olson and M.M. Salama, *Corrosion* **54**(6) (1998) 480.
21. E.P. DeGarmo, J.T. Black and R. Kosher, 'Materials and Processes in Manufacturing', 7th edn. (New York. Macmillan, 1988).
22. H.E. McGannon (Ed.), 'The Making, Shaping and Treating of Steel', 9th edn. (United States Steel, 1971).
23. R.A. Higgins, 'Engineering Metallurgy: Applied Physical Metallurgy', 6th edn. (Arnold, London, 1993).
24. L.E. Samuels, 'Optical Microscopy of Carbon Steels' (ASM, 1980).
25. J.L. Mora-Mendoza and S. Turgoose, *Corros. Sci.* **44** (2002) 1226.